Precipitation hardening and structure evolution in hypereutectic Al-6 % Fe-Zr alloys subjected to ultrasonic melt processing

S. Chankitmunkong [a], F. Wang [b], P. Pandee [c,d], C. Limmaneevichitr [c], D.G. Eskin [e,f,*]

[a] *Department of Industrial Engineering, School of Engineering, King Mongkut's Institute of Technology Ladkrabang, Chalongkrung Road, Ladkrabang, Bangkok 10520, Thailand*

[b] *School of Metallurgy and Materials, University of Birmingham, Birmingham B15 2SE, United Kingdom*

[c] *Department of Production Engineering, Faculty of Engineering, King Mongkut's University of Technology Thonburi, 126 Pracha-Utid Rd., Bangmod, Tungkhru, Bangkok 10140, Thailand*

[d] *Center for Lightweight Materials, Design and Manufacturing, King Mongkut's University of Technology Thonburi, 126 Pracha-Utid Rd., Bangmod, Tungkhru, Bangkok 10140, Thailand*

[e] *Brunel University London, BCAST, Uxbridge, Middlesex UB8 3PH, United Kingdom*

[f] *Tomsk State University, Tomsk 634050, Russian Federation*

ARTICLE INFO

ABSTRACT

The objective of this research was to study the influence of Zr concentration and ultrasonic melt processing (USP) on the microstructure and precipitation hardening of a hypereutectic Al-6% Fe alloy. Such alloys have a good potential in high-temperature, wear-resistant, and conducting applications but suffer from coarse structure and low strength/ductility, which prevents their processing. The microstructure of the studied alloys consisted of primary $Al_{13}Fe_4$ intermetallics and $(Al)+Al_{13}Fe_4$ eutectic colonies, which were successfully refined by adding Zr and performing USP. The mechanisms of USP and Zr were confirmed for the Al-6 % Fe alloys with a range of Zr additions. The structure refinement led to improved hardness and tensile properties of the alloys. All studied alloys demonstrated strong precipitation hardening effect with hardness increasing 4–5 times, reaching 170 HV for the alloy with 0.4 % Zr after annealing at 400 ℃ for 20 hrs. The electrical conductivity increased from 25 % IACS in the as-cast alloy to 40% IACS in the annealed Al-6% Fe-0.4 % Zr alloy. The prime novelty of this work is a considerable increase of hardness upon annealing, i.e. more than 100 HV, in the Al-6 % Fe alloy with only minute traces of Zr (<0.01 %). The precipitation phenomena were investigated by transmission electron microscopy. The precipitation of the semi-coherent $Al_{13}Fe_4$ phase with Zr segregated to its surface was observed for the first time. All studied alloys (with minute and larger Zr additions) showed the precipitation of this phase, while the alloys with the larger amount of Zr also demonstrated the precipitation of the metastable $L1_2$ Al_3Zr phase. Therefore, the properties improvement was attributed to the structure refinement and the formation of Zr-modified $Al_{13}Fe_4$ and Al_3Zr precipitates in the microstructure.

1. Introduction

Hypereutectic Al–Fe alloys attract attention as a new type of aluminum alloys with a potential for commercial applications at room and high temperatures because of their attractive properties such as light weight, low thermal expansion, good thermal stability, wear and corrosion resistance [1]. Such alloys can be used in high-temperature, wear-resistant parts as well as in additive manufacturing. The presence of iron in their composition makes them also important from the recycling point of view with Al scrap as a potential material for making

these alloys. The microstructure consists of Al–$Al_{13}Fe_4$ eutectic colonies and primary $Al_{13}Fe_4$ phase, which is considered as a hard phase thermally stable due to the low diffusivity of Fe in Al. However, making Al-Fe alloys with a high Fe content by casting is still challenging due to the high melting temperature and also coarse primary iron-containing intermetallics that solidify as plates and laths, deteriorating the mechanical properties [2,3]. These particles need to be refined by a combination of techniques such as grain refiners, alloying additions or physical methods of shearing or ultrasonic cavitation. There are reports that additions of Zr, Sc, Sm, Yb modify and refine primary $Al_{13}Fe_4$

---

particles by adsorption to their interface with the aluminum melt [4,5]. Our previous research showed that a hypereutectic Al-4 % Fe alloy with a 0.3 % Zr addition (here and below all compositions are in wt%) produced using ultrasonic melt processing (USP) demonstrated good mechanical properties due to the refinement of hard $Al_{13}Fe_4$ particles as well as eutectic grains [6]. USP introduces tiny cavitation bubbles into the melt that pulsate and implode producing shockwaves and supersonic liquid jets, which affects nucleation on typically not active substrates (e. g., oxides) and fragment the solid phases present in the melt through the well-established mechanisms reviewed elsewhere [7–10].

It was demonstrated that the combined additions of Zr and Ti alongside USP led to structure refinement in a number of Al-based alloying systems [6,8]. The role of Zr was to produce primary Al_3Zr particles that were refined by USP through a combination of heterogeneous nucleation and fragmentation mechanisms [11] and then acted as nucleating substrate for either Al grains or other phases. Smaller amounts of Ti were added to facilitate growth restriction [8] and possibly assisted in fragmentation of Al_3Zr [9]. Note that adding Zr without USP is not very efficient as rather larger primary Al_3Zr particles hardly play any role in nucleation of the subsequently formed phases, only having a negative effect of the properties. To ensure the efficient introduction of Zr and Ti upon USP it was suggested to use a ternary Al-Zr-Ti master alloy manufactured by salt synthesis [12]. In addition to facilitating the structure refinement upon USP, zirconium can effectively contribute to the strength through precipitation (dispersion) hardening. The reaction of Zr with liquid Al is rather sluggish, which results in supersaturation of Zr into the Al solid solution upon solidification. This Zr can then precipitate in a form of metastable $L1_2$ Al_3Zr particles upon annealing at 350–400 °C and efficiently harden the alloy [13,14]. In the previous work [6], we have examined the combined effects of a 0.3 % Zr addition and USP on the structure refinement and hardening of an Al-4 % Fe alloy and discussed the mechanisms involved. The precipitation hardening effect was attributed solely to the precipitation of coherent Al_3Zr particles upon annealing at 450 °C, while the structure refinement was explained by the enhanced nucleation of phases on primary Al_3Zr particles refined by USP.

To the best of our knowledge there were no reports of any substantial hardening by precipitation of Fe-containing phases in aluminum alloys, even after rapid solidification; nor of the interaction between Zr and Fe-containing precipitates. For example, Kimura et al. [15] reported marginal strengthening by unidentified particles with no orientation relationship with the matrix in an Al-3 % Fe alloy after laser powder bed fusion. Pauzon et al. [16] described marginal hardening from plate-like $Al_{13}Fe_4$ precipitates after an LPFB Al-1 % Fe-1 % Zr alloy was annealed at 400 °C for 4 h with no interaction with Zr that formed its own hardening Al_3Zr precipitates. Wang et al. [17] observed Al_6Fe precipitates at grain boundaries and Al_3(Sc, Zr) hardening precipitates in the grain interior after rapid solidification of an Al-5 % Fe-1 % Mg-0.8 % Sc-0.7 % Zr alloy with no interaction between those. This brief overview shows that up to now the precipitation of Fe-containing phases was not considered as a contributing factor to the hardening of Al-Fe alloy, even after rapid solidification. Also, Zr present in these alloys was not found to interact with Al-Fe precipitates.

In this paper we examine the effects of Zr concentration, from minute additions less than 0.01 to 0.4 %, on a concentrated Al-6 % Fe alloy (the more the amount Fe, the more significant the potential benefits of such alloys). The objectives of this paper were to confirm the effects of Zr and USP on the structure development in a more concentrated alloy and examine in detail the precipitation hardening in this alloy as a function of Zr concentration and USP. The additions of Zr were made through a concentrated in-house made Al-Zr-Ti master alloy in combination with USP. Three levels of additions were studied, i.e., trace addition (<0.01 % Zr) and substantial additions (0.2 % and 0.4 % Zr). The microstructure development, phases formed upon solidification and during hardening, tensile properties and electrical conductivity were evaluated and correlated.

2. Experimental procedure

2.1. Experimental alloys preparation

In this study, three experimental alloys were investigated, characterized by nominal compositions of Al-6 % Fe-0.01 % Zr, Al-6 % Fe-0.2 % Zr, and Al-6 % Fe-0.4 % Zr. These alloys also contained trace amounts of Ti, which were introduced through the utilization of a concentrated master alloy, Al-8 % Zr-2 % Ti. The ternary master alloy was prepared by using Al-10 % Zr and Al-10 %Ti commercial master alloys, which were melted together at 900 °C in a SiC crucible and held for 1 h in an induction furnace. After checking the target composition by spark optical emission spectrometry, the melt was cleaned by fluxing and degassing via argon purging and the dross was skimmed, and the melt was poured at 850 °C in a steel mold to produce a master alloy for subsequent use. The experimental alloys were prepared by mixing 99.7 % pure Al and Al-20 % Fe, Al-8 % Zr-2 %Ti master alloys in relevant proportions in a clay-graphite crucible and melting in an electric melting furnace. The chemical composition of each alloy shown in Table 1 was an average from five measurements, determined by spark optical emission spectrometry.

USP was performed in a crucible containing about 800 g of the liquid alloy (crucible size A10: 160 mm in the top outer diameter, 110 mm in the base outer diameter and 200 mm in height) by using a piezoelectric, air-cooled transducer at a power of 1.5 kW, a frequency of 20 kHz and amplitude of 15 μm. The ultrasonic oscillations were introduced into the melt through a Nb sonotrode 20 mm in diameter. The sonotrode tip was pre-heated to 600 °C and submerged into the melt by 5 mm; USP was then applied into the liquid metal in the temperature range 780–730 °C for 60 s while moving the sonotrode around. After that the sonotrode was removed and the melt was then left to solidify in the SiC crucible. The experimental procedure was similar with the alloy without USP only with a not vibrating sonotrode. The cooling rate upon solidification in the crucible was 0.5 °C/s.

2.2. Metallographic and phase analysis

The solidification sequence of phase formation in the Al-6 % Fe with Zr and Ti additions was evaluated using Thermo-Calc software (version 2023b) with a TCAL8 database.

The metallographic specimens were prepared by grinding with sandpaper and then polishing with diamond and oxide polishing suspensions. The grain structure (eutectic colonies) was observed after the specimens were electrochemically etched in Barker's solution (5% HBF_4 water solution) for about 2 min at 20 VDC and then examined in an Olympus microscope under polarized light. The grain/colony size (linear intercept method), area fraction and size of intermetallics were measured by Image J software with statistical analysis.

To identify the phase formation in the alloys, X-ray diffraction (XRD) in a Rigaku smart Lab machine was used with a scan rate of 12°/min on a bulk specimen disc with a thickness of 1 mm. The elemental analysis was performed in a field emission scanning electron microscope (FE-SEM, ThermoFisher Scientific Apreo S) equipped with an energy-dispersive

Table 1
Chemical composition of the experimental alloys.

Alloys	Alloys code	Chemical composition (wt%)*				
		Fe	Zr	Ti	Si	Al
Al-6Fe	6Fe 6Fe-USP	6.01	0.007	-	0.11	Bal.
Al-6Fe-0.2Zr	0.2Zr 0.2Zr-USP	6.10	0.21	0.09	0.09	Bal.
Al-6Fe-0.4Zr	0.4Zr 0.4Zr-USP	5.96	0.39	0.15	0.1	Bal.

* Other trace elements: Cu 0.02%; Mn 0.01%; Mg 0.001%, Ni 0.009%.

(EDS) detector.

After the annealing (precipitation hardening treatment) at 400 ℃ to obtain the peak hardness, specimens were cut from the samples containing trace Zr additions and 0.4 % Zr, and ground to about 100 μm thickness. The foil specimens were then punched to 3-mm diameter disks and further thinned to perforation by a precision ion polishing system (Gatan PIPS Model 691). The specimens were examined in a ThermoFisher Scientific Talos F200X transmission electron microscope (TEM) operated at an accelerating voltage of 200 kV. The composition of the precipitates was also analyzed by EDS using 4 in-column Super-X detectors in the TEM.

2.3. Heat treatment and mechanical properties

The cast alloy samples were annealed in an electric oven with air circulation at temperatures of 375 °C and 400 °C, with a temperature accuracy of ± 2 °C. The selection of the temperature was based on a previous study [18]. The samples were annealed in 3-h steps for up to 30 h and quenched in water after each step for hardness measurements. Specimens were then polished for Vickers microhardness test with a 10 N load and 15 s dwell time by using a Mitutoyo Micro-Vickers hardness tester. At least ten measurements were made on each specimen in the areas of the aluminum solid solution. The electrical conductivity was measured on the surface of the as-cast specimens and after annealing at 400 °C for 20 h by using a TMD 102 EDDY current electrical conductivity meter at a frequency of 90 kHz.

To investigate the tensile properties of the alloys, specimens were prepared from the annealed alloys, which were subjected to peak hardness annealing at 400 °C for 20 h, following the guidelines specified by the ASTM E8 standard. The tensile specimens were cut in the central part of the casting and machined with a gauge length of 25 mm, a gauge width of 6 mm, and a thickness of 6 mm. The ultimate tensile strength (UTS), yield strength (YS) and percentage elongation (%El) were measured using a computerized universal testing machine (Shimadzu AGX-V2 series) at a cross head speed of 1 mm/s at 25 °C. Three samples for each group were tested and the average values of YS, UTS and elongation were determined.

3. Results

3.1. Phase formation and structure characterization of Al-6Fe-based alloys

Fig. 1 shows the sequence of phase formation upon solidification (Scheil approximation) of the alloys Al-6 % Fe-0.2 % Zr-0.1 % Ti (Fig. 1a) and Al-6 % Fe-0.4 % Zr-0.15 % Ti (Fig. 1b). For the purposes of this work, it is important that the USP was performed in the range of

primary solidification of Al_3Zr and $Al_{13}Fe_4$ phases. The results show that in the alloy with 0.2% Zr the solidification starts at 810 °C with the formation of the $Al_{13}Fe_4$ phase and then Al_3Zr is formed from 758 °C, followed by the eutectic reaction starting at 658 °C. In the alloy with 0.4 % Zr, the primary Al_3Zr phase is formed in the temperature range 820–810 °C, then the primary $Al_{13}Fe_4$ phase is formed between 810 and 659 °C. Hence, the USP was performed in the temperature range of 780–730 °C, where the ultrasonic cavitation affected the formation of primary Al_3Zr and $Al_{13}Fe_4$ phases. Below 730 °C the semi-liquid alloy became too mushy to continue USP of the whole volume.

The minute amounts (as calculated by Thermocalc) of Al_8FeSi_2 (0.05 vol.%) and $Al_9Fe_2Si_2$ (0.016 vol.%) may form in these alloys due to the presence of 0.15 % of Si (only 0.1 % Si has been detected in the alloy, see Table 1). These quantities would be undetectable either by XRD or by metallography.

Fig. 2 presents microstructures of as-cast Al– 6% Fe-based alloys with different levels of Zr additions. It can be clearly observed that the microstructure of the Al– 6% Fe alloy (Fig. 2(a)) consist of large lath-like primary $Al_{13}Fe_4$ particles and the eutectic structure of α(Al) + $Al_{13}Fe_4$ and that the primary phase was refined and changed to thinner and shorter plates in the alloys with 0.2 % and 0.4 % Zr as shown in Fig. 2(b) and (c), respectively. After USP, further significant refinement occurred, with very fine structure obtained in the Al-6% Fe-0.4 % Zr alloy (Fig. 2(f)). The quantitative analysis in Supplementary Materials (Fig. S1) confirmed that the size of primary intermetallics decreased from 568 μm to 198 μm in the 6Fe alloy as a result of USP. The smallest primary particles were formed the 0.4-USP alloy, 87 μm.

Fig. 3 displays the grain (eutectic colony) structures of as-cast alloys. The microstructure analysis clearly reveals both dendrites and eutectic structures within the grains (Fig. 3a). With Zr addition (Fig. 3(b, c)), the eutectic grains become more equiaxed and finer. USP caused additional grain refinement, especially in the alloys with 0.2–0.4 % Zr (Fig. 3(e, f)). These data are further quantified in Fig. S2 in Supplementary Materials. The average eutectic grain size of the 6Fe alloy was significantly reduced by a factor of four, from 898 μm to 216 μm as a result of 0.2 % Zr addition and USP (0.2Zr-USP alloy). On the other hand, the addition of Zr promoted the formation of Al dendrites with the resultant coarsening of the eutectic constituents, while USP refined all structure constituents (including Al dendrites/eutectic colonies), which resulted in the refinement of eutectic particles (became finer and shorter) as demonstrated and quantified in Figs. S3 and S4 in Supplementary Materials.

The as-cast structure of the most concentrated alloy 0.4Zr comprised (in addition to the Al solid solution), the primary and eutectic $Al_{13}Fe_4$ phase, primary $Al_3(Zr)$ phase as well as small amount of Al_6Fe phase formed probably during recalescence. The EDS and XRD analyses are given in Supplementary Materials, Figs. S5-S7. A close connection between $Al_3(Zr)$ particles and $Al_{13}Fe4$ particles was observed in the alloy
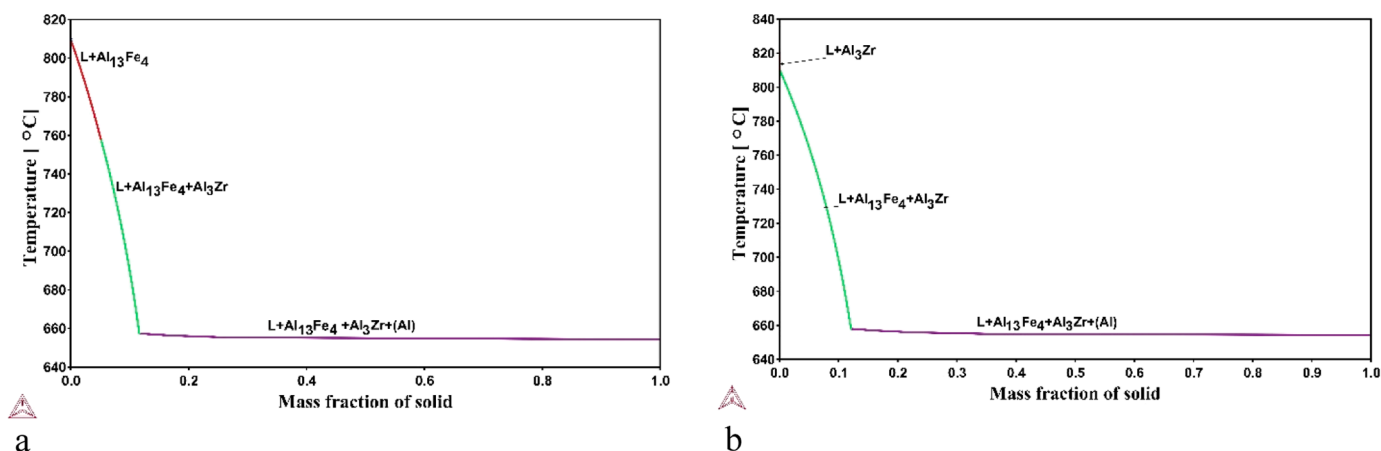

Fig. 1. The sequence of phase formation in Al-6% Fe with (a) 02 % Zr, 0.1 % Ti and (b) 0.4 % Zr and 0.15 % Ti.
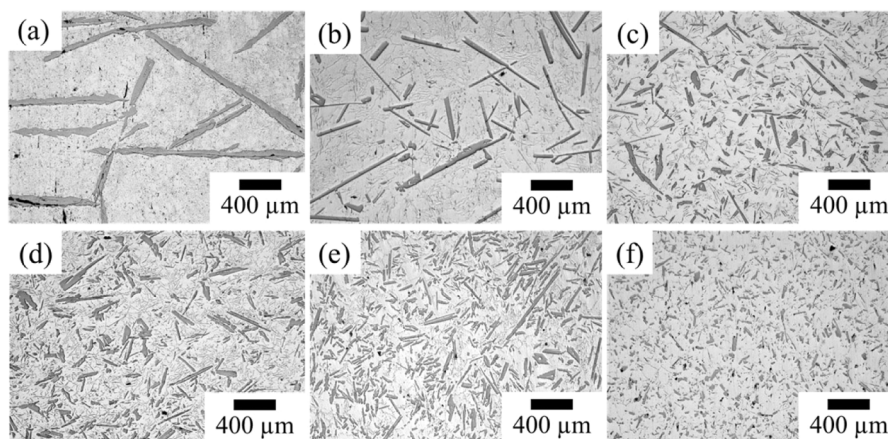
Fig. 2. Microstructure of Al-6Fe alloys: (a) 6Fe, (d) 6Fe-USP, (b) 0.2Zr, (e) 0.2Zr-USP, (c) 0.4Zr and (f) 0.4Zr-USP. For the alloy compositions see in Table 1.
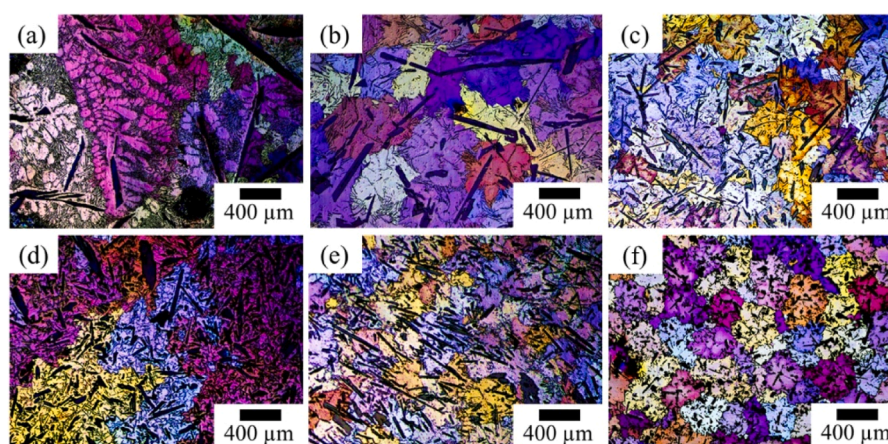

Fig. 3. Grain structure (eutectic colony) of Al-6% Fe-based alloys: (a-c) without USP; (d-f) with USP. (a) 6Fe, (d) 6Fe-USP, (b) 0.2Zr, (e) 0.2Zr-USP, (c) 0.4Zr and (f) 0.4Zr-USP showing the Fe intermetallic refinement.

subjected to USP (Fig. S6).

Fig. 4. Hardness of the as-cast Al-6% Fe-based alloys with different amounts of Zr addition with and without ultrasonic treatment.

3.2. Precipitation hardening and mechanical properties

Fig. 4 displays the hardness of the as-cast Al-6 % Fe-based alloys with different Zr additions, with and without ultrasonic processing. Fig. 5 provides the hardening curves of these alloys at two annealing temperatures. It is noteworthy that the alloys containing Zr and undergoing USP exhibited slightly higher initial hardness levels (Fig. 4). However, upon annealing, the 0.4Zr alloy without USP demonstrated a greater ability for hardening than the same alloy after USP (Fig. 5). The best hardening was demonstrated by the alloy with 0.4 % Zr without USP annealed at 400 °C for about 20–25 h with the hardness going from 34 to 170 HV (more than 5-fold increase).

A very important and surprising observation was that an Al-6% Fe alloy with only trace additions of Zr (6Fe) showed rather strong hardening, which was not expected as iron was not known to form a supersaturated solid solution with aluminum under moderate cooling rates, nor Al-Fe phases cause significant hardening. To demonstrate this observation more clearly, we depicted the hardening curves of the Al-6 % Fe alloys with only trace amounts of Zr in Fig. 6. As one can see the hardness went from 29 to 31 HV to 120–154 HV after annealing at 400 °C for 20 h (4–5-fold increase). A somewhat lesser hardening was observed upon annealing at 375 °C (Fig. 5(a)).

The electrical conductivity of the alloys in the peak hardness condition increased as compared to the as-cast condition (see Fig. S8 in Supplementary Materials), e.g., from 25 % IACS in the as-cast 6Fe alloy to about 40 % IACS in the annealed 0.4Zr-USP alloy.
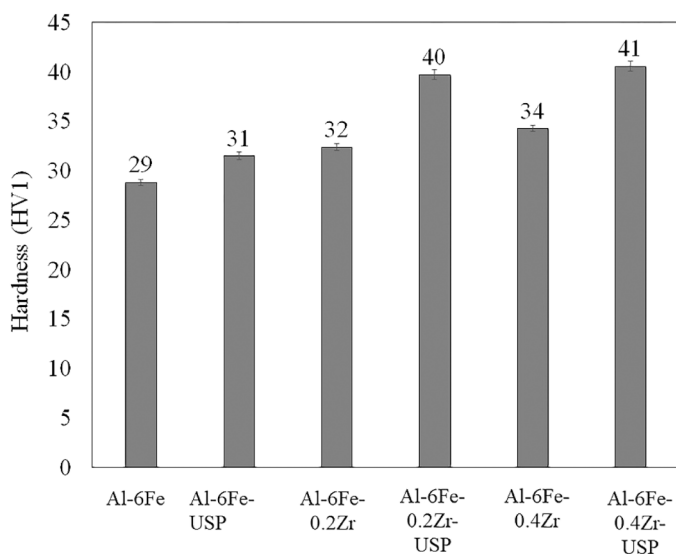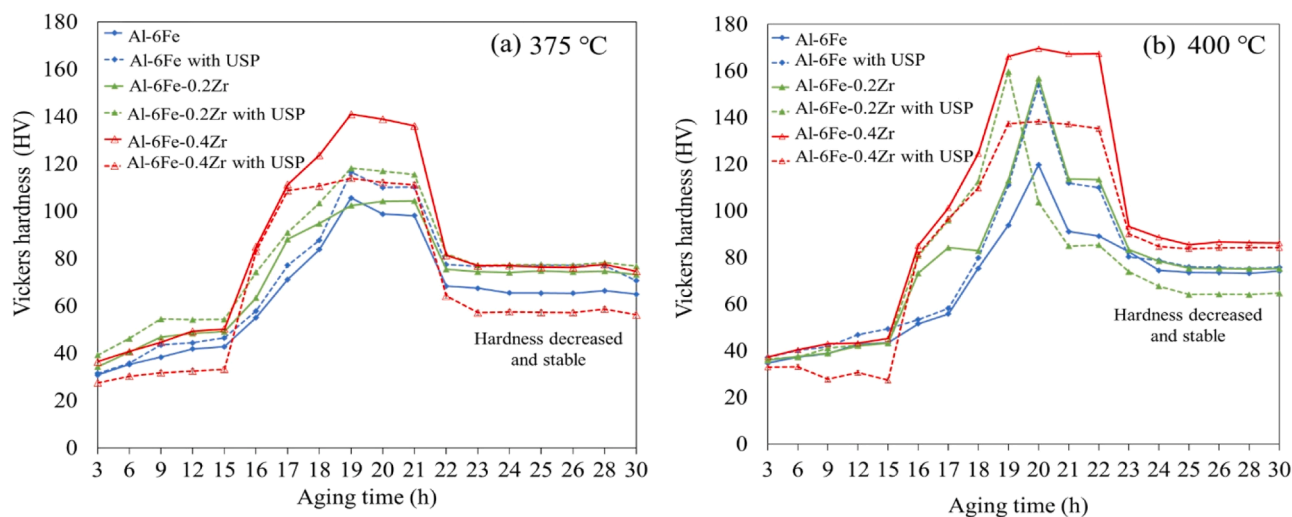
Fig. 5. Hardness of the Al-6% Fe-based alloys with different amounts of Zr addition with and without USP: (a) annealed at 375 ℃ and (b) annealed at 400 ℃. The error bars are smaller than the size of experimental point symbols.
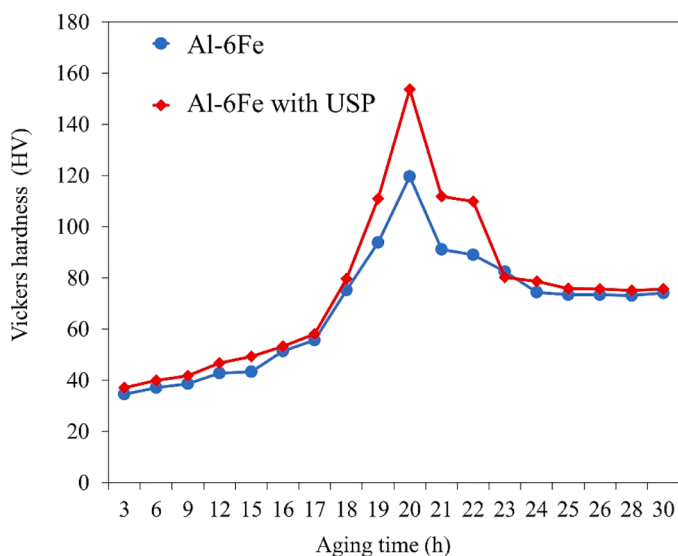

Fig. 6. Hardness change of the 6Fe alloy upon annealing at 400 ℃.

Fig. 7. Tensile properties at room temperature of the Al-6% Fe-based alloys with different Zr additions subjected to USP and annealing at 400 ℃ for 20 h (UTS, YS and %El).

Finally, the tensile properties are given in Fig. 7. There was a consistent increase in the yield and tensile strength as well as the elongation with the increase of Zr addition and USP. The UTS increased more than 20%, the YS more than 25 % and the %El more than 50 %.

4. Discussion

4.1. Confirmation of structure refinement with Zr and USP in concentrated hypereutectic Al-Fe alloys

The USP was performed in the temperature range of solidification of primary $Al_{13}Fe_4$ particles, and resulted in their refinement (Fig. 2(a, d)), while the grain structure remained largely unaffected (Fig. 3(a, d)). The addition of Zr caused significant refinement of the primary $Al_{13}Fe_4$ particles (Fig. 2) and after USP – also considerable refinement of the eutectic grain structure (Fig. 3, S1-S3). As has been found in the previous research [6], this confirms that primary Al_3Zr act as a substrate for $Al_{13}Fe_4$ phase and Al grains/eutectic colonies (and this effect was enhanced upon USP due to the refinement of Al_3Zr as a result of ultrasonic cavitation [10,11]). The confirmed synergy between the Al_3Zr and
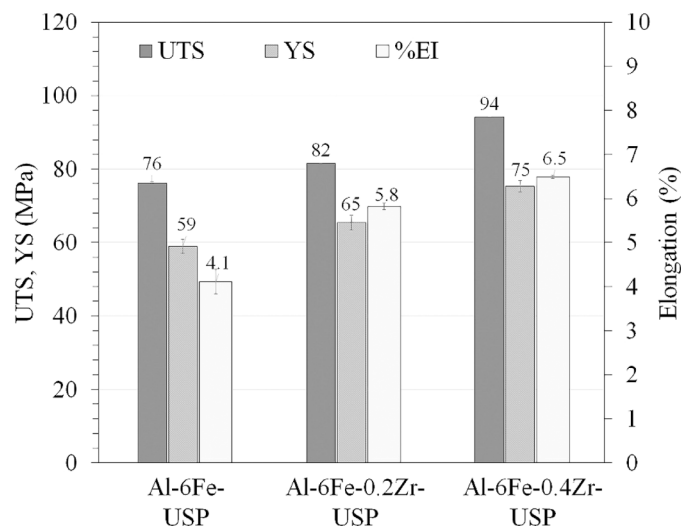
$Al_{13}Fe_4$ particles (Fig. S6) reinforces the suggestion that the refined Al_3Zr phase can be an efficient nucleant for both Al [11] and $Al_{13}Fe_4$ phases [6]. The presence of Ti in the alloys (from the master alloy) did not lead to the formation of an individual phase (Figs. S5, S7), in agreement with the predictions of Thermocalc (Fig. 1). This effect is quite common as the Al_3Ti phase is formed in these alloys though a sluggish peritectic reaction, which can be easily suppressed under real solidification conditions. The same is true for the primary Al_3Zr phase, the formation of which is also frequently suppressed upon solidification, leading to the supersaturation of the Al solid solution. USP, however, triggers the heterogeneous nucleation of the primary phases and promotes the formation of Al_3Zr in these alloys. We have measured by EDS the concentration of Zr in the Al solid solution after solidification in the alloys with 0.4 % Zr and found that the alloy cast without USP had 0.276 % Zr while the alloys cast with USP – only 0.156 % Zr. These findings reflect the enhanced formation of Al_3Zr as a result of USP treatment and also explain why the precipitation hardening in the Zr-containing alloys subjected to USP may be lesser than in the alloys without USP.

The structure formation in the concentrated hypereutectic Al-Fe

alloys containing Zr and subjected to USP was, therefore, confirmed to occur as follows. The formation (albeit sluggish) of Al_3Zr in the alloys with hyper-peritectic concentrations of Zr (0.2 % and 0.4 % in our case) is followed by the primary solidification $Al_{13}Fe_4$. In the case of Al_3Zr formation it acts as a substrate for nucleation of primary $Al_{13}Fe_4$ and eutectic grains. Some of Zr supersaturates the Al solid solution upon solidification. USP performed in the solidification range of Al_3Zr and $Al_{13}Fe_4$ has a dual function. Firstly, it refines the primary Al_3Zr particles by enhancing their nucleation of activated oxides [19], and fragmentation by shock waves emitted by imploding cavitation bubbles [10]. These refined particles apparently act as substrates for nucleation of $Al_{13}Fe_4$ as well as Al and eutectic grains, effectively refining these structure constituents. Due to the enhanced Al_3Zr formation during solidification, the amount of Zr available for supersaturation decreases. Secondly, USP facilitates fragmentation of primary $Al_{13}Fe_4$, leading to the additional refinement of these primary particles. Ti in the alloys remains in the liquid solution or may partially dissolve in the Al_3Zr phase. Its main role is to restrict growth of the primary phases.

4.2. Precipitation hardening with Fe and Zr

The hardening effect in Al-6 % Fe alloys with only trace additions of Zr (Figs. 5 and 6) was a surprise discovery and the primary novelty of this research. Al-Fe alloys are not known for precipitation hardening and even for any measurable supersaturation with Fe, unless they are produced under extreme conditions. Previous works reported supersaturation of the Al solid solution with Fe only after extremely high cooling rates [20,21] or during severe deformation [22] with marginal hardening from precipitation of either Al_6Fe or $Al_{13}Fe_4$ particles at relatively low temperatures, between 100 and 300 °C. The significant hardening observed in this research for the Al-6Fe alloy with only trace concentration of Zr called for a closer examination of the structure and phase composition after annealing.

Fig. 8 demonstrates the precipitation of thin lath-type particles with the length not exceeding 500 nm in the alloy 6Fe. The elemental mapping clearly showed the presence of Fe but also a segregation of Zr at the interface between the precipitate and the Al solid solution.

It is known that Fe can potentially form upon precipitation the equilibrium $Al_{13}Fe_4$ or metastable Al_6Fe phases [23]. Fig. 9 gives the diffraction patterns and interfacial structure of the precipitates observed in in Fig. 8. The selected area diffraction pattern in Fig. 9(b) shows distinct diffraction spots from the precipitates (Fig. 9(a)) in addition to those from the Al matrix.

The *d*-spacing values measured based on SADPs were compared with the standard *d*-spacing values as shown in Table 2.

Comparing the measured *d*-spacing values with those reported for $Al_{13}Fe_4$ and Al_6Fe [23] revealed that they were consistent with those of $Al_{13}Fe_4$. Moreover, the overlapped (matrix and precipitates) diffraction patterns along $Al_{13}Fe_4$ [100] and Al[100] zone axes generated by SingleCrystal software and those obtained in the current work, and the corresponding orientation relationships were compared with those reported for $Al_{13}Fe_4$ and (Al) or for Al_6Fe and (Al) [24,25]. The orientation relationships observed $Al[100]//Al_{13}Fe_4[100]$, $Al(020)//Al_{13}Fe_4(040)$, $Al(002)//Al_{13}Fe_4(006)$ agreed well with those reported between $Al_{13}Fe_4$ and Al and, therefore, the precipitates observed were identified as $Al_{13}Fe_4$ phase. Furthermore, the HRTEM image of the interface between the $Al_{13}Fe_4$ precipitate and (Al) in Fig. 9(c) with the corresponding diffraction pattern in Fig. 9(d), showed good lattice matching (semi-coherent) across the interface, which was consistent with the theoretical calculation of *d*-spacing mismatch as listed in the previous research [25].

With the further addition of Zr, the expected precipitation of the metastable $L1_2$ Al_3Zr phase occurred as evidenced by Fig. 10(a, b) showing the elongated precipitates of $Al_{13}Fe_4$ and the round precipitates of Al_3Zr. The interface between the $Al_{13}Fe_4$ precipitates and the matrix remains semi-coherent (Fig. 10(c)). The diffraction patterns confirmed the formation of the $Al_{13}Fe_4$ phase (Fig. 10(d)) similar to that in the alloy with only trace amounts of Zr (Fig. 9(b, d)) as well as the metastable Al_3Zr phase (Fig. 10(e)). The latter precipitates are likely to be coherent with the matrix having the well-known orientation relationship Al $[100]//Al_3Zr[100]$, $Al(002)//Al_3Zr(002)$. The segregation of Zr to the interface of the $Al_{13}Fe_4$ precipitates was observed in this alloy as well, see Fig. 11. It is worth noting that this segregation might be stronger as compared to the alloy containing only trace amounts of Zr, apparently due to the more Zr available in the solid solution. However, further investigation will be required to explore this phenomenon in detail, and it will be the focus of a subsequent study.

These observations revealed the novel precipitation phenomena in the alloys under study that explained the hardening effects shown in Figs. 5 and 6. There was some supersaturation of the Al solid solution with Fe and a significant supersaturation with Zr upon even slow cooling during solidification. Within this study we could not reliably measure the concentration of Fe in the solid solution, which will be a subject of the next extended study into this phenomenon. However, the clear evidence of $Al_{13}Fe_4$ precipitation indicated that the supersaturation with Fe indeed happened. Therefore, there were two systems of hardening precipitates in the Al-Fe alloys with Zr: thin semi-coherent laths of $Al_{13}Fe_4$ and spherical coherent precipitates of metastable Al_3Zr. We can
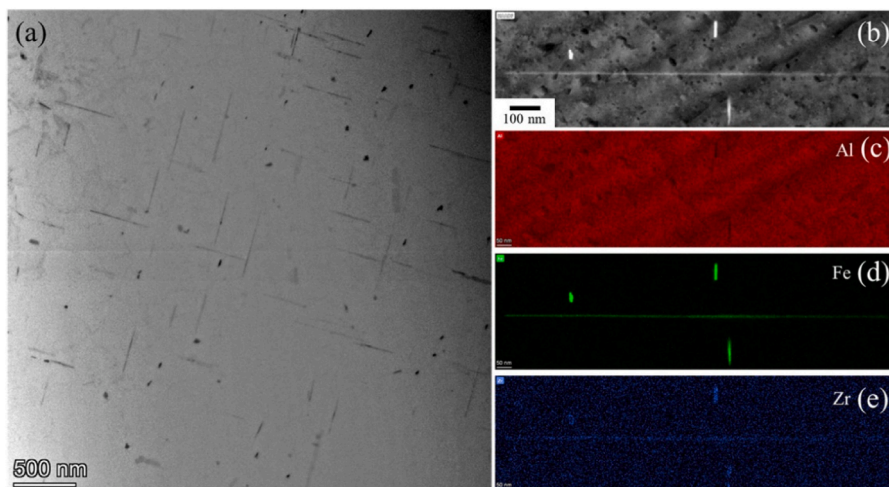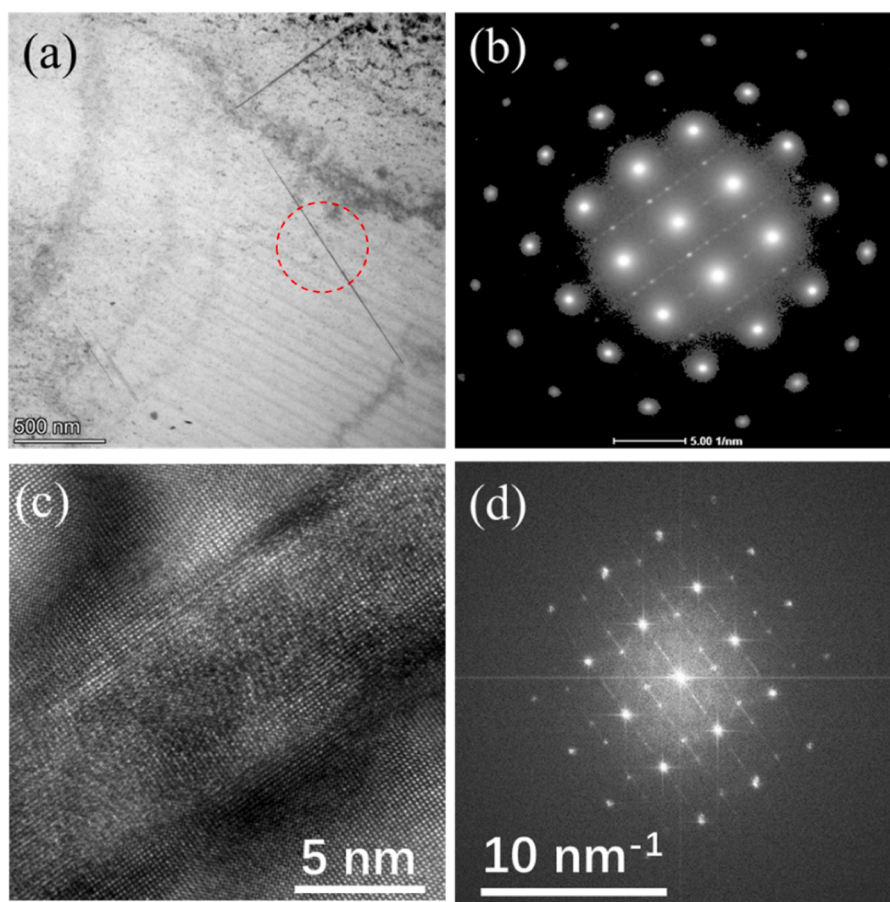

Fig. 8. TEM images of the 6Fe alloy (0.007% Zr) annealed at 400 °C for 20 h: (a) bright field image of the precipitates, (b) HAADF-STEM image of representative precipitates, and EDS mapping of the element distributions: (c) Al, (d) Fe and (e) Zr.

Fig. 9. Phase composition of the 6Fe alloy (0.007% Zr) annealed at 400 °C for 20 h: (a) a bright field image of the precipitates; (b) selected area diffraction patterns obtained from the area highlighted by red circle in (a); (c) HRTEM image of the interface between the $Al_{13}Fe_4$ precipitate and Al matrix; (d) FFT of the HRTEM image in (c).

Table 2
Comparison of measured and standard interplanar spacing for the planes along [100] $Al_{13}Fe_4$.

| Plane Indexes	Measured d-spacing (nm)	Standard d-spacing (nm)
{040}	0.2058	0.2021
{0$\bar{2}$1}	0.3788	0.3826
{0$\bar{2}$2}	0.3363	0.3342
{0$\bar{2}$3}	0.2819	0.2829
{0$\bar{2}$4}	0.2383	0.2394
{0$\bar{2}$5}	0.2058	0.2049

only speculate at the moment that the segregation of Zr to the interface of the $Al_{13}Fe_4$ precipitates enhanced their hardening ability either through modifying the interfacial structure or energy. Previous studies of precipitation in Al-Fe-Zr alloys did not report anything similar [16, 26]. A clue maybe found in a very recent study on the precipitation phenomena in the Al-Sc-Zr system [27] that reported the formation of a new phase due to the presence of trace Fe impurity. In difference to the $Al_{13}Fe_4$ phase detected in our study, the phase in ref. [27] was pseudo-icosahedral with apparent five-fold symmetry, and rich in Fe. The similarity with our case is in the segregation of Zr (and Sc) to the interface between this phase and the matrix, forming the outside layer with an $L1_2$ structure. The layered structure allowed complete coherency with the aluminum matrix. Therefore, in our case, the Zr-rich layer on the $Al_{13}Fe_4$ precipitates may actually resemble the structure of the $L1_2$ Al_3Zr phase promoting the coherency with the matrix and improving the hardening ability of these precipitates. Other papers [4,5]

reported segregation of transition elements like Zr, Sc, Sm, Yb to the interface of the $Al_{13}Fe_4$ phase with liquid aluminum, so this type of segregation may have a general character, not limited to the solid state.

To the best of our knowledge, it is the first observation of the phenomenon that encompasses the precipitation of the hardening $Al_{13}Fe_4$ phase in alloys produced at moderate cooling rates, and the segregation of Zr to its interface with the matrix, potentially affecting its coherency and hardening ability. This phenomenon will be thoroughly investigated in the subsequent research, aiming at comprehensive understanding of its mechanisms and implications.

As we already mentioned the amount of Zr in the supersaturated solid solution was lower in the alloys subjected to USP due to the enhanced formation of primary Al_3Zr that consumed Zr potentially available for supersaturation. This agrees well with the observed lesser hardening effect (Fig. 5) and higher electrical conductivity (Fig. S8) in these alloys.

The synergetic effect of structure refinement (both primary and grain structure) and precipitation hardening led to an improvement of mechanical properties in the alloys with high concentration of Zr subjected to USP (Fig. 7). The simultaneous increase in the tensile strength and ductility was likely due to the formation of more evenly distributed hard and refined structure constituents, which resulted in a more even stress distribution without obvious stress concentration upon deformation and, therefore, in the delayed fracture. This phenomenon is well known in composite alloys [28,29].
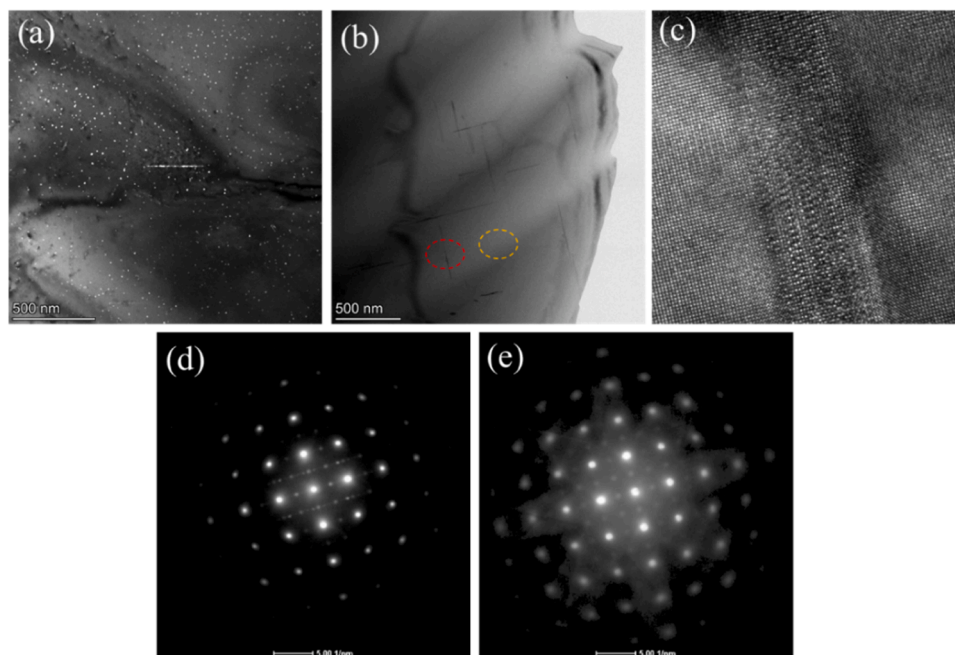
Fig. 10. Precipitation in the 0.4Zr alloy annealed at 400 °C for 20 h: (a) dark field image of precipitates; (b) bright field image of precipitates; (c) HRTEM image of the interface between an $Al_{13}Fe_4$ precipitate and the Al matrix; (d) selected area diffraction pattern obtained from the area highlighted by red circle in (b), and (e) selected area diffraction pattern obtained from the area highlighted by yellow circle in (b).
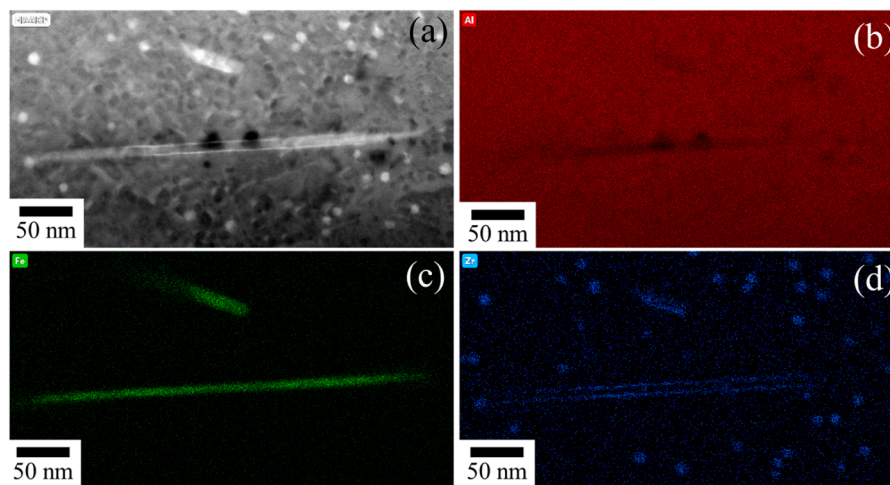
Fig. 11. (a) HAADF STEM image of precipitates in the 0.4Zr alloy annealed at 400 °C for 20 h, and EDS mapping of the element distributions: (c) Al, (d) Fe and (e) Zr.

5. Conclusions

We studied the microstructure evolution and precipitation hardening in Al-6% Fe-based alloys with Zr solidified with and without ultrasonic melt processing. The effect of USP and Zr on microstructure evolution led to improved hardness, tensile properties and electrical conductivity, though the USP may result in less hardening due to a lesser amount of Zr available in the supersaturated solid solution. We revealed a new phenomenon of precipitation hardening in these alloys resulted from the formation of semi-coherent $Al_{13}Fe_4$ precipitates with Zr segregated to their interface with the matrix. The key conclusions can be drawn as follows:

1. The addition of 0.2–0.4 % Zr to a hypereutectic Al-Fe alloy led to the formation of primary Al_3Zr phase that acted as a substrate for the nucleation of primary $Al_{13}Fe_4$ and eutectic grains. Ultrasonic melt

processing resulted in further refinement of all structure constituents. Although reported in our previous work, these observations confirm the universal nature of these mechanisms for a wider range of hypereutectic Al-Fe alloys with Zr.

2. The improved mechanical properties of annealed Al-6% Fe alloys even with small Zr additions resulted from the synergetic effect of structure refinement (both primary and grain structure) and precipitation hardening.

3. The strengthening in Al-Fe alloys with Zr additions occurred through a combined precipitation of thin semi-coherent $Al_{13}Fe_4$ plates and spherical coherent metastable Al_3Zr precipitates.

4. The segregation of Zr to the interface of $Al_{13}Fe_4$ precipitates was observed for the first time and may explain the enhanced hardening by $Al_{13}Fe_4$ in these alloys, even with minute Zr additions. This new phenomenon opens a new route in alloy development and applications, from conventional casting to additive manufacturing.

CRediT authorship contribution statement

S. Chankitmunkong: Funding acquisition, Data curation, Formal analysis, Writing - original draft, Writing - review & editing. **F. Wang**: Data curation, Writing - review & editing. **P. Pandee:** Data curation. **C. Limmaneevichitr**: Funding acquisition, Writing - review & editing. **D. G. Eskin:** Conceptualization, Funding acquisition, Formal analysis, Writing - original draft, Writing - review & editing.

Declaration of Competing Interest

The authors declare that they have no known competing financial interests or personal relationships that could have appeared to influence the work reported in this paper.

Data availability

Data will be made available on request.

Acknowledgments

Appendix A. Supporting information

Supplementary data associated with this article can be found in the online version at doi:10.1016/j.jallcom.2023.172613.

References

[1] X.P. Niu, L. Froyen, L. Delaey, C. Peytour, Effect of Fe content on the mechanical alloying and mechanical properties of Al-Fe alloys, J. Mater. Sci. 29 (1994) 3724–3732, https://doi.org/10.1007/BF00357340.

[2] J. Chen, R. Lengsdorf, H. Henein, D.M. Herlach, U. Dahlborg, M. Calvo-Dahlborg, Microstructure evolution in undercooled Al–8 wt%Fe melts: comparison between terrestrial and parabolic flight conditions, J. Alloy. Compd. 556 (2013) 243–251, https://doi.org/10.1016/j.jallcom.2012.11.182.

[3] P.R. Goulart, J.E. Spinelli, N. Cheung, A. Garcia, The effects of cell spacing and distribution of intermetallic fibers on the mechanical properties of hypoeutectic Al–Fe alloys, Mater. Chem. Phys. 119 (1) (2010) 272–278, https://doi.org/10.1016/j.matchemphys.2009.08.063.

[4] K. Dai, J. Ye, Z. Wang, M. Gao, J. Chen, R. Guan, Effects of Sc and Zr addition on the solidification and mechanical properties of Al–Fe alloys, J. Mater. Res. Technol. 18 (2022) 112–121, https://doi.org/10.1016/j.jmrt.2022.02.070.

[5] L. Mo, M. Jiang, X. Zhou, Y.-J. Zhao, J. Du, Modification mechanisms of hypereutectic Al-Fe alloys treated by Sm/Yb addition: experiments and first-principles calculations, J. Alloy. Compd. 948 (2023) 169786, https://doi.org/10.1016/j.jallcom.2023.169786].

[6] S. Chankitmunkong, D.G. Eskin, C. Limmaneevichitr, Structure refinement, mechanical properties and feasibility of deformation of hypereutectic Al–Fe–Zr and Al–Ni–Zr alloys subjected to ultrasonic melt processing, Mater. Sci. Eng. A 788 (2020), 139567, https://doi.org/10.1016/j.msea.2020.139567.

[7] G.I. Eskin, D.G. Eskin. Ultrasonic Treatment of Light Alloy Melts, second ed., CRC Press,, Boca Raton, 2015.

[8] T.V. Atamanenko, D.G. Eskin, L. Zhang, L. Katgerman, Criteria of grain refinement induced by ultrasonic melt treatment of aluminum alloys containing Zr and Ti, Metall. Mater. Trans. A 41 (8) (2010) 2056–2066, https://doi.org/10.1007/s11661-010-0232-4.

[9] T.V. Atamanenko, D.G. Eskin, M. Sluiter, L. Katgerman, On the mechanism of grain refinement in Al–Zr–Ti alloys, J. Alloy. Compnd. 509 (1) (2011) 57–60, https://doi.org/10.1016/j.jallcom.2010.09.046.

[10] A. Priyadarshi, M. Khavari, S.B. Shahrani, T. Subroto, L.A. Yusuf, M. Conte, P. Prentice, K. Pericleous, D. Eskin, I. Tzanakis, In-situ observations and acoustic measurements upon fragmentation of free-floating intermetallics under ultrasonic cavitation in water, Ultrason. Sonochem. 80 (2021), 105820, https://doi.org/10.1016/j.ultsonch.2021.105820.

[11] W. Feng, D. Eskin, T. Connolley, J.-W. Mi, Influence of ultrasonic treatment on formation of primary Al₃Zr in Al–0.4 Zr alloy, Trans. Nonferrous Met. Soc. China 27 (5) (2017) 977–985, https://doi.org/10.1016/S1003-6326(17)60115-8.

[12] V. Sreekumar, D. Eskin, A new Al-Zr-Ti master alloy for ultrasonic grain refinement of wrought and foundry aluminum alloys, JOM 68 (12) (2016) 3088–3093, https://doi.org/10.1007/s11837-016-2120-x.

[13] K.E. Knipling, D.C. Dunand, D.N. Seidman, Nucleation and precipitation strengthening in dilute Al-Ti and Al-Zr alloys, Metall. Mater. Trans. A 38 (10) (2007) 2552–2563, https://doi.org/10.1007/s11661-007-9283-6.

[14] K.E. Knipling, D.C. Dunand, D.N. Seidman, Precipitation evolution in Al–Zr and Al–Zr–Ti alloys during isothermal aging at 375–425°C, Acta Mater. 56 (1) (2008) 114–127, https://doi.org/10.1016/j.actamat.2007.09.004.

[15] T. Kimura, T. Nakamoto, T. Ozaki, T. Miki, Microstructures and mechanical properties of aluminum-transition metal binary alloys (Al-Fe, Al-Mn, and Al-Cr) processed by laser powder bed fusion (LPBF), J. Alloy. Compd. 872 (2021), 159680, https://doi.org/10.1016/j.jallcom.2021.159680].

[16] C. Pauzon, M. Buttard, A. Després, B. Chehab, J.-J. Blandin, G. Martin, A novel laser powder bed fusion Al-Fe-Zr alloy for superior strength-conductivity trade-off, Scr. Mater. 219 (2022), 114878, https://doi.org/10.1016/j.scriptamat.2022.114878.

[17] Y. Wang, R. Li, T. Yuan, L. Zou, M. Wang, H. Yang, Microstructure and mechanical properties of Al-Fe-Sc-Zr alloy additively manufactured by selective laser melting, Mater. Character 180 (2021), 111397, https://doi.org/10.1016/j.matchar.2021.111397.

[18] N. Belov, A. Alabin, D. Eskin, V. Istomin-Kastrovskii, Optimization of hardening of Al–Zr–Sc cast alloys, J. Mater. Sci. 41 (2006) 5890–5899, https://doi.org/10.1007/s10853-006-0265-7.

[19] J.G. Jung, Y.H. Cho, S.-D. Kim, S.B. Kim, S.H. Lee, K. Song, K. Euh, J.M. Lee, Mechanism of ultrasound-induced microstructure modification in Al–Zr alloys, Acta Mater. 199 (2020) 73–84, https://doi.org/10.1016/j.actamat.2020.08.025.

[20] A. Tonejc, X-ray study of the decomposition of metastable Al-rich Al-Fe solid solutions, Metall. Trans. 2 (1971) 437–440, https://doi.org/10.1007/BF02663331.

[21] D. Kunstelj, A. Bonefačić, Decomposition of a supersaturated aluminum-rich aluminum-iron solid solution during annealing, Metallography 3 (1) (1970) 79–87, https://doi.org/10.1016/0026-0800(70)90007-8.

[22] J.M. Cubero-Sesin, Z. Horita, Age hardening in ultrafine-grained Al-2 pct Fe alloy processed by high-pressure torsion, Metall. Mater. Trans. A. 46A (2015) 2614–2624, https://doi.org/10.1007/s11661-015-2876-6.

[23] C.A. Aliravci, M.Ö. Pekgüleryüz, Calculation of phase diagrams for the metastable Al-Fe phases forming in direct-chill (DC)-cast aluminum alloy ingots, Calphad 22 (2) (1998) 147–155, https://doi.org/10.1016/S0364-5916(98)00020-0.

[24] N.A. Belov, A.A. Aksenov, D.G. Eskin, Iron in Aluminium Alloys: Impurity and Alloying Element, CRC Press, Boca Raton, 2002.

[25] P. Liu, G.L. Dunlop, Crystallographic orientation relationships for Al-Fe and Al-Fe-Si precipitates in aluminium, Acta Met. 36 (6) (1988) 1481–1489, https://doi.org/10.1016/0001-6160(88)90215-5.

[26] J. Ye, R. Guan, H. Zhao, A. Yin, Effect of Zr content on the precipitation and dynamic softening behavior in Al–Fe–Zr alloys, Mater. Character 162 (2020), 110181, https://doi.org/10.1016/j.matchar.2020.110181.

[27] T. Dorin, S. Babaniaris, L. Jiang, A. Cassel, A. Eggeman, J. Robson, Precipitation sequence in Al-Sc-Zr alloys revisited, Materialia 26 (2022), 101608, https://doi.org/10.1016/j.mtla.2022.101608.

[28] Z. Zhang, G. Chen, S. Zhang, Y. Zhao, R. Yang, M. Liu, Enhanced strength and ductility in ZrB₂/2024Al nanocomposite with a quasi-network architecture, J. Alloy. Compd. 778 (2019) 833–838, https://doi.org/10.1016/j.jallcom.2018.11.214.

[29] E. Ma, T. Zhu, Towards strength–ductility synergy through the design of heterogeneous nanostructures in metals, Mater. Today 20 (6) (2017) 323–331, https://doi.org/10.1016/j.mattod.2017.02.003.